










RESEARCH ARTICLE | AUGUST 23 2019

X-ray sources using a picosecond laser driven plasma accelerator

Special Collection: [Papers from the 60th Annual Meeting of the APS Division of Plasma Physics](#)

N. Lemos ; P. King ; J. L. Shaw; A. L. Milder; K. A. Marsh; A. Pak; B. B. Pollock; C. Goyon ;
W. Schumaker; A. M. Saunders ; D. Papp ; R. Polanek; J. E. Ralph; J. Park ; R. Tommasini;
G. J. Williams ; Hui Chen; F. V. Hartemann; S. Q. Wu; S. H. Glenzer ; B. M. Hegelich ; J. Moody;
P. Michel; C. Joshi; F. Albert



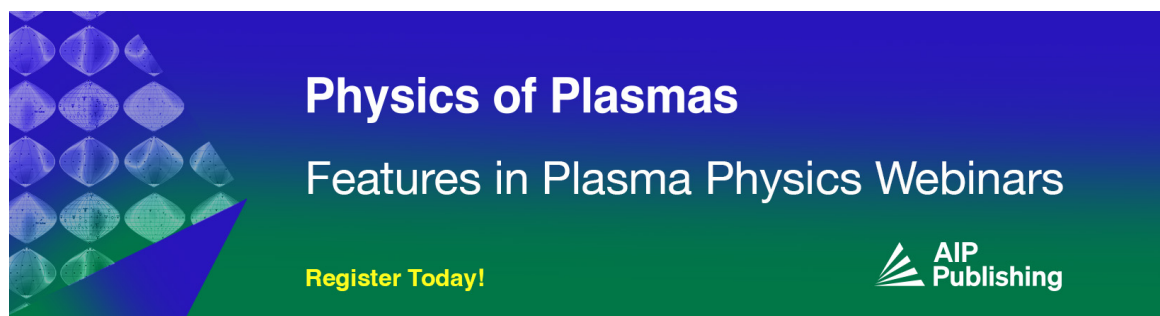
Physics of Plasmas 26, 083110 (2019)

<https://doi.org/10.1063/1.5091798>

 CHORUS




CrossMark



Physics of Plasmas
Features in Plasma Physics Webinars

Register Today!



X-ray sources using a picosecond laser driven plasma accelerator

Cite as: Phys. Plasmas **26**, 083110 (2019); doi: 10.1063/1.5091798

Submitted: 5 February 2019 · Accepted: 2 May 2019 ·

Published Online: 23 August 2019



View Online



Export Citation



CrossMark

N. Lemos,^{1,a)} P. King,^{1,2} J. L. Shaw,³ A. L. Milder,³ K. A. Marsh,⁴ A. Pak,¹ B. B. Pollock,¹ C. Goyon,¹ W. Schumaker,⁵ A. M. Saunders,¹ D. Papp,⁶ R. Polanek,⁶ J. E. Ralph,¹ J. Park,¹ R. Tommasini,¹ G. J. Williams,¹ Hui Chen,¹ F. V. Hartemann,¹ S. Q. Wu,¹ S. H. Glenzer,⁵ B. M. Hegelich,² J. Moody,¹ P. Michel,¹ C. Joshi,⁴ and F. Albert¹

AFFILIATIONS

¹Lawrence Livermore National Laboratory, NIF and Photon Sciences, 7000 East Avenue, Livermore, California 94550, USA

²Department of Physics, University of Texas at Austin, Austin, Texas 78712, USA

³Laboratory for Laser Energetics, University of Rochester, 250 E River Rd., Rochester, New York 14623, USA

⁴Department of Electrical Engineering, University of California Los Angeles, 405 Hilgard Ave., Los Angeles, California 90095, USA

⁵SLAC National Accelerator Laboratory, Stanford, California 94309, USA

⁶ELI-ALPS, ELI-HU Non-Profit Ltd., Szeged 6728, Hungary

Note: This paper is part of the Special Collection: Papers from the 60th Annual Meeting of the APS Division of Plasma Physics.

Note: Paper B13 2, Bull. Am. Phys. Soc. **63** (2018).

^{a)}Invited speaker.

ABSTRACT

Laser-plasma-based accelerators are now able to provide the scientific community with novel high-energy light sources that are essential to study high-energy density matter, inertial confinement fusion, astrophysical systems, and fundamental plasma physics. Due to the transient and high-density properties of these systems, it is essential to develop light sources that are in the hard x-ray energy range (0.01–1 MeV) and directional and have high yield, low divergence, and short duration (ps and sub-ps). In this work, we show that by using a Laser plasma accelerator, it is possible to generate a broadband (0.01–1 MeV) hard x-ray source that satisfies the previous requirements. A series of experiments were conducted on the Titan laser at the Lawrence Livermore National Laboratory where a 10 nC electron beam in the 10–380 MeV energy range was generated through a laser plasma accelerator. The electrons generate x-rays via their betatron motion (few–30 keV) and hard x-rays through inverse Compton scattering (10–250 keV) and/or Bremsstrahlung (up to 1 MeV). Due to its unique characteristics, this source can be an important tool for many applications in large-scale international laser facilities.

Published under license by AIP Publishing. <https://doi.org/10.1063/1.5091798>

I. INTRODUCTION

X-ray beams in the keV to MeV energy range are essential to study high energy density (HED) matter and to improve the understanding of inertial confinement fusion,¹ astrophysical systems,² and fundamental plasma physics. HED experiments produce highly transient matter under extreme states of temperatures and pressures that are often probed using either broadband Bremsstrahlung x-rays^{3–7} or narrow band x-ray line radiation^{8–13} emitted by a hot plasma created by an auxiliary laser pulse. These sources are quasi-isotropic; therefore, most of the x-ray photons are not intercepted by the target and they often lack the spatial resolution to resolve μm size features. A reproducible, directional, and easily deployable x-ray source in the 10 keV–1 MeV energy range with a high-spatial resolution is desirable

for HED science applications. X-rays sources based on laser plasma accelerators (LPA) are attractive for this purpose; they are highly directional and can resolve μm size features.^{14–17} Great effort has been put in developing such sources using fs long laser pulses, but these sources cannot yet meet the needs of many single-shot HED experiments. The physics of x-ray emission from laser wakefield acceleration in the picosecond, kilojoule-class regime is largely unexplored and has the potential to satisfy the HEDS (High Energy Density Science) source needs. A LPA driven by such laser pulses can generate highly relativistic, low-divergence electron beams^{18–21} with 10's of nC s of charge. This represents a two order of magnitude increase in charge when compared to LPA's driven by fs laser pulses. The peak electron beam current in this work is ~ 15 kA, which is approximately what is reached in LPAs

driven by fs laser pulses. Although we reach the same current value as LPA's driven by fs laser pulses, there are applications that will directly benefit from the higher electron beam charge produced by LPAs driven by ps laser pulses, such as electron beam imaging of HED conditions²² and generation of high yield x-rays sources. Hence, these LPA electrons can generate high-energy, high-yield, low-divergence, broadband x-rays with tens of μm s spatial resolution using three different processes: Betatron radiation,¹⁶ Inverse Compton scattering (ICS) radiation,^{23–25} and Bremsstrahlung radiation.¹⁷ In this paper, we compare and review the x-ray beam characteristics and explore the optimization of these three mechanisms. We show that each one of these processes has different energy spectra, sources sizes, and divergences that can be controlled by carefully tuning the LPA and choosing the targets. We show that we produced a high-energy x-ray source with an unmatched combination of photon flux and source size that in the future can be coupled to HED facilities and enable unique HED science applications, such as imaging of double shell implosions,²⁶ precision MeV-radiography,^{3,4} or phase contrast imaging of laser-driven shocks at high energy.^{27–30} Despite the fact that current LPA x-ray sources driven by fs lasers have very high brilliances (three orders of magnitude higher than the ones present here), they do not have the necessary photon yields to address these applications. The sources presented here have a one order of magnitude lower brilliance but produce one to two orders of magnitude more photons while maintaining the necessary spatial and temporal resolution that is ideal for the above-mentioned applications. When a high-intensity ($>10^{18}$ W/cm²) laser pulse with a 1 ps duration such that its length ($\sim 300 \mu\text{m}$) is larger than the plasma period ($\sim 30 \mu\text{m}$ for a 10^{18} cm⁻³ electron density) is focused onto an underdense target, it can generate plasma waves through Raman Forward Scattering (RFS).¹⁸ The background plasma electrons that have the correct momentum and phase will “surf” this wave and gain energy up to hundreds of MeV. Moreover, the long laser pulse will overlap many plasma periods as well as the accelerating electrons, further accelerating the electrons through direct laser acceleration (DLA).^{31–34} During this process, due to the transverse restoring forces inside the plasma waves, the electrons undergo transverse oscillations emitting x-ray betatron radiation.¹⁶ It has been shown that betatron radiation driven by ps, kJ-class lasers can generate a high-yield x-ray source with photon energies up to a few tens of keV.¹⁹ To increase the yield of the high energy photons (>50 keV), we explored the ICS mechanism. In this case, as the laser beam exits the underdense target, it collides with a plasma mirror (PM),³⁵ which reflects the laser beam backward onto the high-energy electron beam and generates a bright x-ray beam via ICS. This configuration has been shown to work operating in the blowout LPA regime driven by fs lasers,^{36,37} but not in the LPA regime driven by ps lasers. The ps regime will benefit from a 1–2 orders of magnitude increase in electron beam charge and a longer interaction time with the laser pulse. Combining these two effects, we observe a three order of magnitude increase in the photon yield when compared to the LPA regime driven by fs lasers. To further increase the yield of high-energy x-rays (>250 keV), the plasma mirror is replaced with a high-Z foil, changing the dominant mechanism for x-ray production to bremsstrahlung radiation from the relativistic electrons colliding with the foil.²⁰ This paper is organized as follows. In Sec. II, a brief background of x-ray generation by LPA is given. In Sec. III, the experimental setup is described. The experimental results for the electron and x-rays are presented in Sec. IV. The conclusions are presented in Sec. V.

II. BACKGROUND: LPA AS AN X-RAY SOURCE

A. Betatron radiation

Betatron radiation has mainly been studied using Joule-class, sub-100-fs duration laser beams¹⁵ or highly relativistic electron beams.³⁸ A recent study¹⁹ explores the possibility of using kilojoule-class, ps-duration laser pulses to drive a hybrid-LPA to increase the number of generated photons. It was shown that at a photon energy of 6.5 keV, a photon yield of 1.45×10^{12} photon/keV/Sr was measured, representing a three order of magnitude increase compared to the best results using fs, J-class lasers.¹⁵

Here, a high-intensity ($>1 \times 10^{19}$ W/cm²) laser pulse with a pulse duration, τ_p , much larger than the plasma period, λ_p/c (c is the speed of light), propagates through an underdense plasma and generates plasma waves through the Raman Forward Scattering (RFS) and self-modulation (SM) instabilities¹⁸ of the laser pulse (Fig. 1 - front part of the accelerator). Once the plasma waves are driven to wave-breaking limits,³⁹ they can trap the background electrons and accelerate them to hundreds of MeV energies through the associated longitudinal fields. These waves also have associated transverse fields that will lead to betatron-like oscillations of the trapped off-axis electrons, causing them to radiate x-rays photons in the forward direction (Fig. 1). Furthermore, the electrons undergoing betatron oscillations in the polarization plane of the laser will feel the electric field of the laser. Since the laser pulse overlaps many plasma wavelengths (30 plasma periods for a plasma density of 1×10^{19} cm⁻³ and a laser pulse duration of 1 ps) and therefore the accelerating electrons, there is a significant contribution from DLA to the energy gained by the electrons⁴⁰ that further increases the x-ray energies and yield. Thus, the LPA is operating in a hybrid regime, where both laser wakefield acceleration and DLA contribute to the energy gained by the electrons. A recent publication⁴⁰ shows that the electrons accelerated in the front part of an LPA driven by a ps laser pulse with a normalized laser vector potential, $a_0 = 3$, (with $a_0 = 8.5 \times 10^{-10} \lambda[\mu\text{m}]^{1/2} [\text{W}/\text{cm}^2]$ and λ is

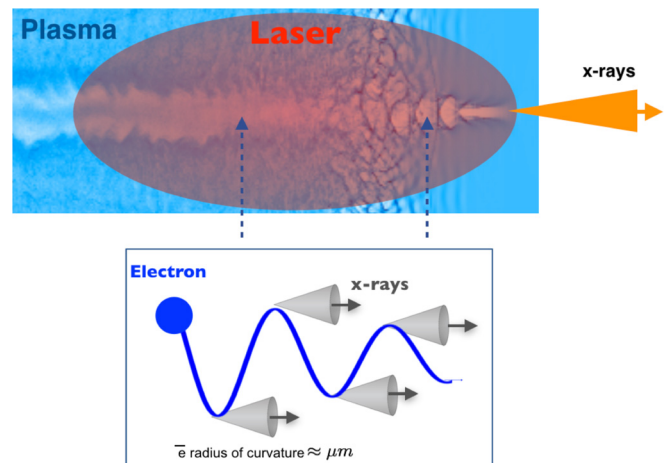


FIG. 1. Schematic of the generation of betatron radiation from an LPA driven by a 100 J, 1 ps laser. The laser is represented in red, and the electron plasma density in blue. The electrons will execute betatron motion in the front region of the LPA, where the dominant acceleration mechanism in wakefield as well as at the back of the pulse, where the dominant acceleration mechanism is DLA emitting x-ray radiation.

the laser wavelength) are mainly accelerated by the wakefield longitudinal electric field (Fig. 1). At the back of the laser pulse, due to the formation of an electron cavitation region caused by the radially moving ions, the plasma waves are weak, and the electrons are mainly accelerated by DLA (Fig. 1). Nevertheless, the electrons in both regions will undergo transverse betatron oscillations emitting synchrotron radiation driven by these acceleration mechanisms. The intensity distribution dI per unit photon energy, dE , and solid angle, $d\Omega$ of the emitted synchrotron radiation can be approximated by⁴⁰

$$\frac{d^2I}{dEd\Omega} \propto A \left(\frac{E}{E_c}\right)^2 K_{2/3}^2[E/E_c], \quad (1)$$

where A is the spectral amplitude, E is the photon energy, $K_{2/3}$ is the modified Bessel function, and $E_c \propto \gamma^2 n_e r_b$ is the critical energy of the betatron spectrum. Here, γ is the electron relativistic factor, n_e is the plasma density, and r_b is the radius of oscillation of the electron. The divergence of the x-ray beam can be approximated by $\theta \propto r_b \sqrt{n_e/\gamma}$ and the total number of photons can be approximated by $N_\gamma \propto N_e N_b r_b \sqrt{\gamma n_e}$, where N_e is the total number of electrons and N_b is the number of betatron periods. When driving an LPA with a ps, kJ-class laser,¹⁹ the electron beam charge is increased by two orders of magnitude, contributing to an increase in the number of emitted photons.

B. Bremsstrahlung radiation

Bremsstrahlung radiation from an LPA was first demonstrated by colliding an electron beam driven by a 80 J, 1 ps duration laser beam, into a 1.75 mm-thick tantalum foil⁴¹ (Fig. 2).

This scheme has two main advantages when compared to the classic laser-solid bremsstrahlung sources: the electron beam has a low divergence (mrad), which reduces the divergence of the bremsstrahlung emission, and the electron beam can reach higher energies (MeV-GeV) thus generating higher-energy bremsstrahlung photons. In this approach, the laser beam and the electron exit the LPA and collide with a high-Z material, generating a bright x-ray beam (Fig. 2). A high-Z material is used to increase the Bremsstrahlung conversion efficiency due to the high-charge nuclei. As the electrons pass near the

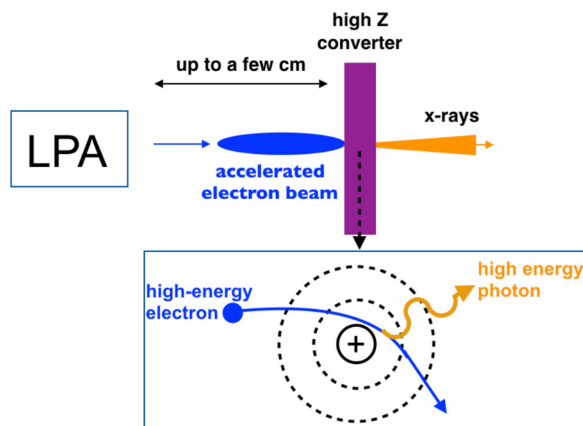


FIG. 2. Schematic of the generation of bremsstrahlung radiation driven by an electron beam from an LPA.

nucleus of the material, they are slowed down as their path is deflected. Due to energy conservation, the lost energy is emitted as a high-energy photon (Fig. 2). Typically, bremsstrahlung spectra can be approximated by

$$\frac{d^2I}{dEd\Omega} \propto B e^{-E/E_T}, \quad (2)$$

where B is the peak spectral amplitude, E_T is the temperature of the exponentially decaying Bremsstrahlung spectrum, and E is the photon energy. The maximum energy of the Bremsstrahlung spectrum matches the maximum energy of the electron beam, since if the electron comes to a total stop, it will transfer all of its energy into a photon. With fs laser pulses, this scheme has produced directional, broadband hard x-ray sources with fs time resolution and tens of microns spatial resolution.¹⁷ However, the photon yield for single-shot HEDS applications is still too low, due to the low charge electron beams (hundreds of pC s). In recent work,²⁰ the electron beam charge has been increased to tens of nC by driving an LPA with a ps, kJ-class laser, which increases the x-ray yield by two orders of magnitude.

C. Inverse Compton scattering radiation

ICS sources based on LPA have been developed using fs long laser pulses mainly using two schemes: a PM or a secondary counter-propagating laser pulse.⁴² In the PM scheme, as the laser beam exits the LPA, it collides with a low-Z material foil placed at the exit of the LPA. This collision creates a plasma mirror,³⁶ which reflects the laser beam backward onto the high-energy electron beam and generates a bright x-ray beam via ICS (Fig. 3). This method offers an exceptionally compact, self-aligned, inexpensive, simple way to convert even the smallest LPAs into robust ICS sources. The other approach is to use a secondary laser beam that counter-propagates with the electron beam. Both of these schemes have a number of advantages when compared to classical ICS schemes (where the electron beam is produced by a Linac),³⁸ such as: a small facility size (small room), pulse duration on the order of the laser pulse duration (fs to ps), jitter-free

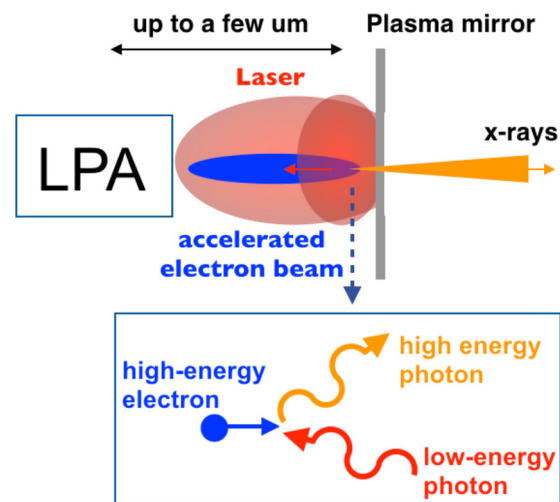


FIG. 3. Schematic of the generation of ICS radiation driven by an electron beam from an LPA.

27 July 2023 08:47:43

synchronization between the x-ray probe and the laser pump pulses, controllable bandwidth with tunable photon energy, micron-scale source size, and small mrad divergences.

Great effort has been put in developing ICS sources using fs-long laser pulses, but the physics of x-ray emission from LPA in the pico-second, kilojoule-class regime is largely unexplored. Using a ps-kJ class laser and the PM scheme, we show a three orders of magnitude increase in the photon yield, achieving for the first time the necessary yield to start addressing HED applications. This configuration has been shown to work operating in the blowout LPA regime (fs laser pulse length, 1/2 plasma period)³⁶ but never in the hybrid-LPA regime driven by ps, kJ lasers. In this regime, it will benefit from the two orders of magnitude increased electron beam charge and the longer interaction time with a ps laser pulse. ICS occurs when an electron collides with a photon and transfers part of its energy to the recoiled photon. This occurs when the electron energy is much larger than the photon energy in the rest frame and the electron experiences a negligible recoil. When the laser a_0 is much larger than one, the electron can absorb several photons, and this process is referred to as nonlinear ICS. When the laser a_0 is smaller than one, the electron only absorbs a single photon and this process is referred to as linear ICS. In this paper, we are operating in the linear ICS regime since the counter-propagating laser has an a_0 of one. Considering a head-on collision between an electron and a photon, the photon energy of the scattered photon is given by two successive Doppler shifts: first from the lab frame to the electron frame and then back to lab frame. Thus, the maximum scattered photon energy is given by $4\gamma^2 E_L$,²³ where E_L is the photon energy. In this geometry the x-ray pulse duration is given by τ_e

+ $\tau_L/4\gamma^2$,⁴³ where τ_e is the electron beam duration and τ_L is the laser pulse duration. Since γ is relatively high in the hybrid LPA, the ICS x-ray beam duration is primarily determined by the electron beam duration. The number of scattered photons per laser period and per electron can be approximated by $1.53 \times 10^{-2} a_0^2$ and the x-ray beam divergence by a_0/γ .¹⁵ In our hybrid-LPA, where we generate an exponentially decaying electron energy spectrum, the ICS spectrum can be approximated by a similar energy distribution given by

$$\frac{d^2 I}{dE d\Omega} \propto \sum C_i e^{-E/E_{T_i}}, \quad (3)$$

where C_i is peak spectral density and E_{T_i} is the temperature of the exponentially decaying spectrum. As it is shown in Sec. IV,²¹ the final spectrum can be approximated by a sum of several exponential functions with different temperatures.

III. EXPERIMENTAL SETUP

In this paper, we will report on three different experiments that used small variations of the setup presented in Fig. 4. Specific details of each setup can be found in Ref. 19 for the betatron radiation experiment, Ref. 20 for the bremsstrahlung experiment and Ref. 21 for the ICS experiment. The experiments have been performed at the Jupiter Laser Facility at the Lawrence Livermore National Laboratory.

The laser beam was produced by a Nd:glass chirped pulse amplification laser system with an energy of 120 J (on target), an average pulse duration of 1 ps (FWHM), and a central wavelength of 1053 nm. The main beam was focused with a $f/10$ off-axis parabola (OAP), 100 μm to 1 mm inside a 3 or 4-mm wide column of gas created by a

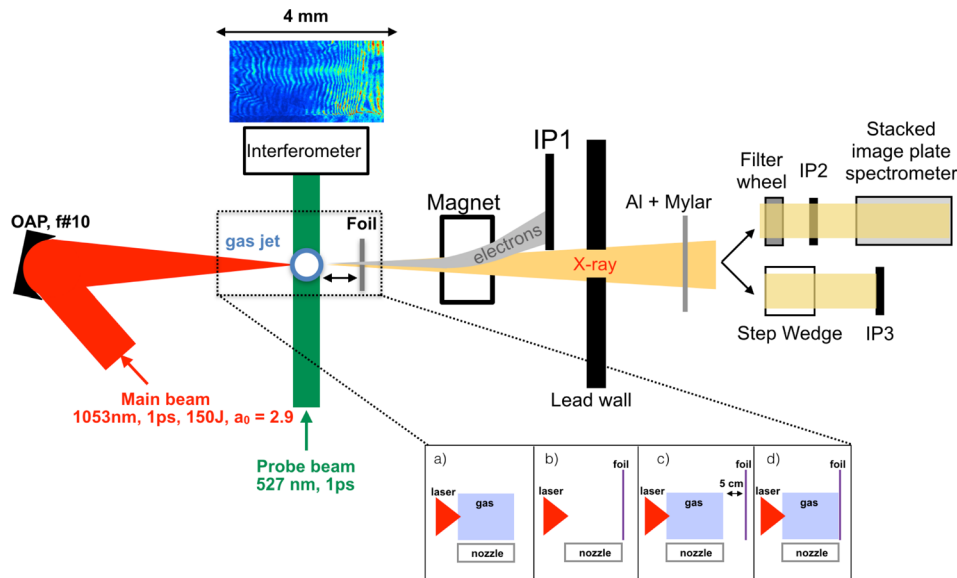


FIG. 4. Experimental setup at the Jupiter Laser Facility using the Titan Laser. The Titan laser (red beam) is focused by an OAP into a 3–4 mm supersonic gas jet. The probe beam (green beam) crosses the plasma generated by the main beam and goes into a folded interferometer. An example interferogram is shown next to the interferometer. The electrons are dispersed by a permanent magnet centered on the laser axis and recorded into an image plate IP1. A foil placed at a distance d from the nozzle exit is used to produce x-rays either through ICS or bremsstrahlung. To produce and characterize betatron radiation, the foil is removed. A lead wall with an opening after the gas jet blocks the background noise generated inside the chamber. At the exit of the vacuum chamber, the x-rays (brown line) go through an Aluminum and Mylar filter. After exiting the vacuum chamber, the x-rays propagate through the filter wheel and stacked image plate spectrometer or through a 36 step wedge filters onto the IP3. We show configurations to measure (a) the betatron radiation, (b) the laser bremsstrahlung radiation, (c) the electron bremsstrahlung radiation, and (d) the ICS radiation.

supersonic nozzle.^{44,45} The gas composition for each shot could be varied from pure He to He/N₂ mixtures containing between 1% and 100% N₂ (by partial pressure) to take advantage of ionization injection.⁴⁶ The vacuum spot size w_0 was 29 μm measured with low laser power at the $1/e^2$ intensity point. The peak intensity was 2×10^{19} W/cm² and the normalized vector potential a_0 of the laser pulse was 3. The 527-nm, 1 ps FWHM probe beam crossed the main beam transversely and was timed to arrive just after the main beam exits the gas jet into a folded interferometer⁴⁷ used to measure the plasma electron density profile, shape, and length. Interferometry measurements indicate that the typical plasma electron density profile consisted of a 500- μm density up and down-ramp with a 2000 to 3000- μm plateau (for the 3 mm and 4 mm nozzles, respectively) with a density $n_e = 1\text{--}15 \times 10^{18}$ cm⁻³. The electrons accelerated in the gas jet (grey beam) exit the gas jet and collide with a foil placed at a distance d after the nozzle to generate an x-ray beam either through bremsstrahlung or ICS. The betatron radiation is generated in the LPA, so in this case no foil was placed at the exit of the gas jet. The electron beam is dispersed into an image plate (IP1) by a 1 T dipole magnet for the ICS and bremsstrahlung experiments and by a 0.42 T dipole magnet for the betatron radiation experiment, to characterize the electron beam spectrum and charge. The x-rays pass through an opening in the lead wall that blocks the background noise generated inside the vacuum chamber and exits the chamber through an Aluminum and Mylar window. Outside the chamber, three different diagnostics are used to characterize the x-ray beam. For x-rays energies between 5 and 90 keV, a combination of a filter wheel and a stacked-image-plate spectrometer⁴⁸ is used and for energies of 80 to 800 keV a High-Energy Differential-Filtering Photon Spectrometer⁴⁹ is used. The low energy x-rays cross through the filter wheel, consisting of 10 or 15 (two different filter wheels were used) concentric filter wedges arranged as Ross-pairs (RRs), and are recorded by IP2. The remaining x-ray signal continues into a stacked-image-plate spectrometer to characterize photons with energies from 20 to 500 keV. The high-energy photons (90–1000 keV) are measured with a High-Energy Differential-Filtering Photon Spectrometer, which has an array of 36 different filters of Ta and Al with variable thickness, and are recorded by IP3. The angle covered by any of the three diagnostics is ~ 9 mrad, smaller than the divergence of any of the x-ray sources and that of the electron beam. The photon energy spectra presented in this paper are analyzed using three different methods that were applied to each of the three diagnostic when possible: Forward fit method (FF),¹⁹ which fits a predetermined function to the transmission signal of the filters that constitute the diagnostic; Ross pair (RP) analysis⁵⁰ of the paired materials; and Differential Averaged Transmission (DAT) analysis³⁶ through the several filters. A final result for the energy spectrum results from the combination of these three methods with the associated error bars.⁵¹ A detailed description of how these methods are applied to these particular diagnostics has been recently published.⁵¹

IV. EXPERIMENTAL RESULTS

A. Electron beam characterization

Characterizing the electron beams from the LPA is extremely important since it will dictate the characteristics of the later generated x-ray beams. To characterize the electron beam energy spectrum, divergence, shape, and charge, the foil after the nozzle was removed to avoid beam distortions. Different nozzles were used in the three

experimental campaigns. For the betatron radiation campaign, a 3 mm nozzle was used and for the integrating current transformer (ICT) and bremsstrahlung campaigns, a 4 mm nozzle was used. A typical electron energy spectrum is shown in Fig. 5 for an electron density of 5×10^{18} cm⁻³ using a 4 mm He gas jet. The electron spectrum maximum energies varied from 200 to 380 MeV, depending on the nozzle and plasma density used.

The electron spectrum displays the typical exponentially decaying energy distribution with a two-temperature distribution $N_e \propto e^{-E/T_1} + e^{-E/T_2}$, where T_1 ranged from 7 MeV to 18 MeV and T_2 from 20 to 50 MeV, depending on the nozzle and plasma density used. The electron beam shape was measured without the electron spectrometer, and an example is shown in the inset of Fig. 5. The electron beam shows an ellipticity in the direction of the laser polarization with an average FWHM divergence of $100 \times 64 \pm 10$ mrad. This ellipticity has been observed before and can be attributed to the residual transverse momentum that the electrons gain at the moment of ionization and/or to DLA.^{31,52,53} The divergence of the electron beam increased with the plasma density, and for plasma densities larger than 2×10^{19} cm⁻³, it loses the beam-like shape with divergences too large to be measured by our diagnostics. The total charge of the electron beam is measured with an integrating current transformer (ICT) placed 50 cm after the nozzle and without the electron spectrometer. The average total charge varied from 4 to 11 nC per shot for electron energies above 10 MeV, depending on the plasma density and nozzle length.

B. Betatron source characterization

The betatron radiation was produced and measured using the experimental configuration shown in Fig. 4(a) and using a 3 mm nozzle.¹⁹ To characterize the x-ray spectrum for photon energies < 30 keV, we utilize the signal record on IP2 after the photons pass through the filter-wheel composed of 15 filters. The signal was analyzed using the methods in Ref. 51 where the fitting function used is given by Eq. (1). In addition, some of the filters are organized as Ross Pairs providing a direct measurement of the x-ray photon yield at a specific energy band. The measured critical energies (E_c) ranged from

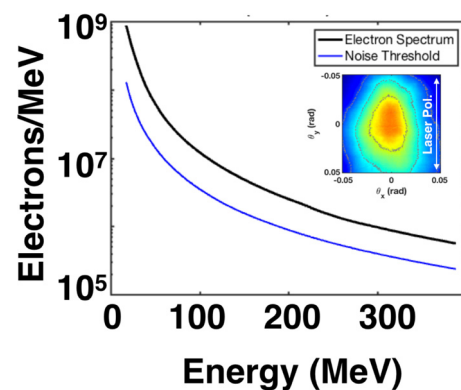


FIG. 5. Typical measured electron beam spectrum (black curve) for a plasma density of 5×10^{18} cm⁻³ in He 4 mm gas jet. The blue line represents the background noise level on IP1. The inset shows a typical electron beam shape without the dispersion magnet where the black lines represent the contour of the encircled energy for 25%, 50%, and 75% from smaller to larger radius, respectively.

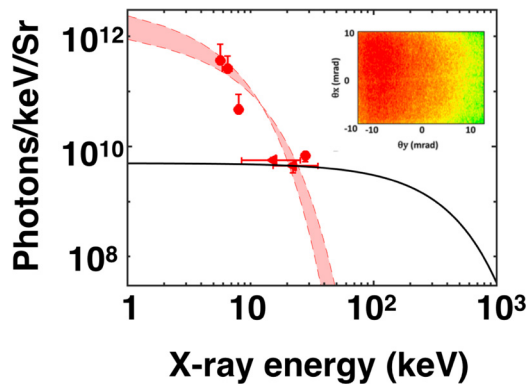


FIG. 6. Deduced x-ray spectra for the betatron signal (red) and Bremsstrahlung signal (black). The red circles represent the Ross-pair points and the triangles the points from the DAT method. These spectra were obtained with a laser $a_0 = 3$ and in a 3 mm He gas jet with plasma density of $1 \times 10^{19} \text{ cm}^{-3}$. The inset shows a partial betatron beam shape recorded by IP2 on an equivalent shot.

10 to 40 keV depending on the plasma densities $0.5\text{--}1.5 \times 10^{19} \text{ cm}^{-3}$ and the laser $a_0 = 1.4\text{--}3.0$. Figure 6 shows an example of a measured experimental x-ray spectrum with a critical energy of 10 keV (red curve).

Using the Ross-pair differential signal, we measured an x-ray photon yield of $0.3\text{--}1.45 \times 10^9$ photons/eV/Sr at 6.5 ± 0.5 keV for an a_0 of 1.44 and 3, respectively. To quantify the x-ray spectrum at photon energies between 10 and 500 keV, we use the stacked image plate spectrometer. Applying the same analysis fitting method revealed that the signal was too noisy to fit a single betatron function. We assumed that this noise was caused by the lower energy (<500 keV) electrons being strongly deflected by the magnet and colliding into the walls of the target chamber, generating an extra bremsstrahlung x-ray signal. Therefore, in addition to the betatron fitting function, we added an additional bremsstrahlung function given by Eq. (2). During the fitting process, the betatron E_c was set to the value given by the filter wheel (10 keV) and the best fit is obtained for an $E_T = 200$ keV. This showed that the bremsstrahlung signal dominated the x-ray spectrum for energies above 40 keV as seen in Fig. 6 (black curve). The x-ray beam shape was recorded on IP2 by removing the filter wheel (inset in Fig. 6), and the divergence was calculated by fitting the signal to a 2D Gaussian function that revealed divergencies of 100–200 mrad depending on the plasma density and laser a_0 used. To measure the source size, a sharp, stainless-steel edge was placed 22 cm after the nozzle and the filter wheel removed, casting a clear shadow on IP2. The measured $1/e^2$ source diameter had an upper bound of $35 \mu\text{m}$.

C. Electron bremsstrahlung source characterization

The electron bremsstrahlung radiation was produced and measured using the experimental configuration shown in Fig. 4(c) using a 4 mm nozzle. The electrons accelerated in the gas jet (grey beam) exit the gas jet, collide with a metal foil placed 1.5 cm after the nozzle, and generate an x-ray beam through bremsstrahlung. During this experimental campaign, the plasma density was kept constant at a value of $5 \times 10^{18} \text{ cm}^{-3}$ in order to have a low divergence electron beam as the one shown in the inset of Fig. 5. Two foil materials were used:

Tungsten (W) with thicknesses of 0.5 or 1 mm and Tantalum (Ta) with a 1 mm thickness. We expected to generate high-energy x-rays with this configuration, so the High-Energy Differential-Filtering Photon Spectrometer was used to characterize the x-ray energy spectra. In this particular experimental configuration, there are three distinct physical mechanisms that contribute to the x-ray spectrum: betatron radiation from the LPA, bremsstrahlung radiation from the laser hitting the foil, and bremsstrahlung radiation from the electron beam crossing the foil. Thus, to independently characterize each one of these mechanisms, we adapted the experimental setup accordingly.

The bremsstrahlung radiation caused by the laser hitting the foil is characterized by firing the laser without any gas and directly heating the foil. No signal was recorded on IP2 since the laser intensity is four orders of magnitude lower once it gets to the foil 1.9 cm away from focus. To characterize the betatron radiation, the foil was removed and a filter-wheel with 10 concentric filter wedges arranged as Ross-pairs was used to record the signal. Here, the filter wheel diagnostic is used since the expected x-ray energies are too low to be properly characterized by the High-Energy Differential-Filtering Photon Spectrometer. Using the same fitting methods used in the Sec. IV B, a betatron spectrum with an E_c of 18 ± 10 keV and an $A = 5 \times 10^9$ photons/keV/Sr is obtained (Fig. 7). It is important to notice that in this case the betatron mechanism was not optimized, hence the lower yield when compared to the one generated by the betatron-only experiment (Fig. 6). In this case, we used a lower plasma density to reduce the electron beam divergence, thus reducing the divergence of the x-ray source. When the foil is in place, the betatron radiation does not have enough high energy photons to make it through, so the only mechanism that can cross the foil and be detected by IP3 is the bremsstrahlung radiation caused by the electrons crossing the foil. To analyze the data on IP3,⁵¹ we assumed the fitting function given by Eq. (2). Figure 7 shows the obtained spectrum for a foil of 1 mm W (blue curve and points), 1 mm Ta (green curve and points), and 0.5 mm W (black curve and points). Here, we can compare the effect of materials for a given thickness plus the effect of thickness for a given material. The spectrum temperature and amplitude is higher for the W foil (1978 ± 534 keV) than for the Ta foil (1420 ± 300 keV). A small difference in amplitude and temperature is to be expected because the bremsstrahlung cross section directly depends on Z , and with such uncertainty in the measurement,

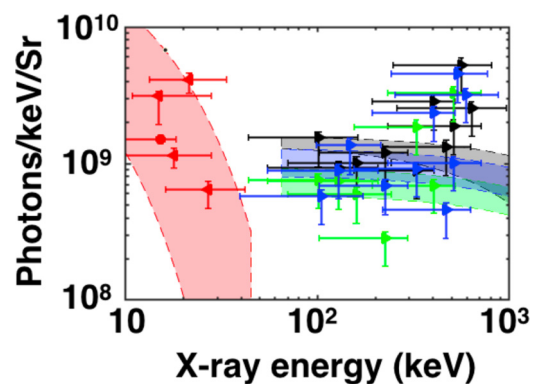


FIG. 7. X-ray energy spectrum for the 1 mm (blue) and 0.5 mm (black) W and 1 mm (green) Ta foils, and the betatron radiation (red). The points represent the measured yield using the DAT method.

this difference cannot be measured experimentally. The bremsstrahlung produced with the 0.5 mm W foil has a lower temperature spectrum than with the 1 mm W foil. With the thinner foil, lower energy electrons have a higher contribution to the spectrum lowering the spectrum temperature. Also, the 0.5 mm W foil has a higher yield for the lower energy photons because these can make it out of the target before being absorbed, unlike for the 1 mm W foil. Experimental measurements of source size and divergence were not possible, but Ref. 20 shows Monte-Carlo simulation results for these quantities using GEANT 4. An x-ray source size of $0.95 \text{ mm} \times 1.5 \text{ mm}$ was inferred (which matches the size of the electron beam on the foil) as well as a divergence of 12.4° (half angle at half-maximum).

D. Inverse Compton scattering source characterization

The ICS radiation was produced and measured using the experimental configuration shown in Fig. 4(d) using a 4 mm nozzle. As the laser beam exits the underdense target, it collides with a $100 \mu\text{m}$ Polyethylene foil placed at the exit. The collision creates a plasma mirror, which reflects the laser beam backward onto the high-energy electron beam and generates a bright x-ray beam via ICS. The plasma density is kept constant at a value of $5 \times 10^{18} \text{ cm}^{-3}$ in order to have a low divergence electron beam (to increase the overlap of the laser and electrons) as the one shown in the inset of Fig. 5. In the setup shown in Fig. 4(d), the observed x-ray signal has contributions from four different mechanisms: betatron radiation from the LPA, bremsstrahlung radiation from the electrons passing through the foil, bremsstrahlung radiation from the laser colliding with the foil, and ICS of the electrons colliding with the laser reflected by the foil. To isolate and characterize the ICS contribution to the final spectrum, measurements of the contribution of each of these mechanisms to the final signal were made by changing the experimental setup as shown in Figs. 1(a)–1(d) [details can be found in Ref. 21].

It was found that the betatron and the bremsstrahlung radiation from the electrons passing through the foil was negligible to the final x-ray signal.²¹ Figure 8 shows in black the x-ray spectrum of the bremsstrahlung radiation generated by the laser colliding with the foil

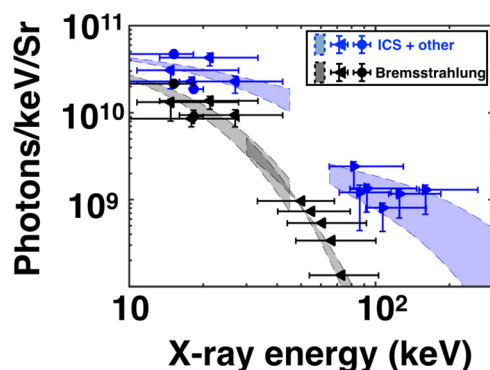


FIG. 8. X-ray energy spectra of the experimental configurations shown in Fig. 4(d) (blue) and Fig. 1(b) (black). The black shaded region and black points (circles - RP, triangles - DAT) show the measured x-ray spectrum for the laser bremsstrahlung radiation. The blue shaded region and blue points (circles - RP, triangles - DAT) show the measured x-ray spectrum when the betatron, bremsstrahlung, and ICS mechanisms are present.

[using the setup in Fig. 4(b)] and in blue the spectrum when all four mechanisms are present [using the setup in Fig. 4(d)]. The spectrum up to photon energies of 40 keV is measured using the filter wheel. For higher photon energies, the bremsstrahlung spectrum is measured using the stacked image plate spectrometer. In the case where all the mechanisms are at play, the High-Energy Differential-Filtering Photon Spectrometer was used since it was less sensitive to background noise generated by the electrons colliding with the chamber walls. From Fig. 8, it is possible to see that at photon energies of 10 keV, the ICS contribution is on the order of the bremsstrahlung radiation generated by the laser colliding with the foil but at 40 keV is already an order of magnitude higher, indicating that the ICS mechanism becomes the dominant process for photon energies higher than 10 keV. Using Eq. (3), it was found that the ICS spectrum was best fitted with a sum of two exponential functions with $E_{T1} = 55 \pm 15 \text{ keV}$ for photon energies between 10 and 40 keV and with $E_{T2} = 100 \pm 20 \text{ keV}$ for photon energies between 80 and 250 keV. A total number of 10^{11} photons per shot were generated representing an improvement of three orders of magnitude when compared to the ICS LPA results obtained in the blowout regime.³⁶ To have an estimate of the x-ray source size, a sharp Ta plate was placed just after the electron beam spectrometer. The filter wheel was removed, and a sharp shadow of the plate was cast onto IP2. Measuring the gradient of the edge shadow, the source size was estimated to be $50 \mu\text{m}$ (measured over $1/e^2$). The x-ray beam shape was also imaged at IP2, showing a divergence of 100 mrad (measured over $1/e^2$) in the horizontal direction (perpendicular to the laser polarization). The vertical divergence could not be measured since the window at the chamber exit only had a 2.5 cm opening.

V. CONCLUSIONS

In this work, we explored x-ray sources from an LPA driven by a ps, kJ-class laser. In a series of three experiments, we generated and characterized x-rays from betatron radiation, electron bremsstrahlung radiation and inverse Compton scattering. For the betatron radiation, we have generated a broadband x-ray spectrum with a yield of 10^9 Photons/eV/Sr at a photon energy of 6.5 keV that is comparable to or better than the bremsstrahlung emission produced from foils at the same laser facility^{54,55} and to the flux of high-Z-plasma M-band emission successfully used for single-shot x-ray absorption near edge structure (XANES).⁵⁶ This source has a divergence of 100 mrad and a source size smaller than $35 \mu\text{m}$. This was the first experimental result generating betatron radiation in such an LPA regime, demonstrating the potential of these sources for undertaking future applications at larger-scale laser facilities. Furthermore, future improvements to this source can still be achieved and a possible route toward a higher yield is to increase the interaction length by increasing the nozzle diameter or by using a long gas cell. Bremsstrahlung radiation was generated by colliding the high-charge electron from the LPA into a tungsten or tantalum foil. We have demonstrated the production of hard x-rays with temperatures from 0.8 to 2 MeV and up to 10^9 Photons/keV/Sr, which represents an improvement of at least two orders of magnitude in the number of photons when compared to the LPA in the blowout regime. According to Monte-Carlo simulations, the estimated x-ray source size was $1 \times 1.5 \text{ mm}$ with a divergence of 12.4° . It was shown that the photon distribution temperature and flux can be controlled by changing the beam electron temperature or target thickness and

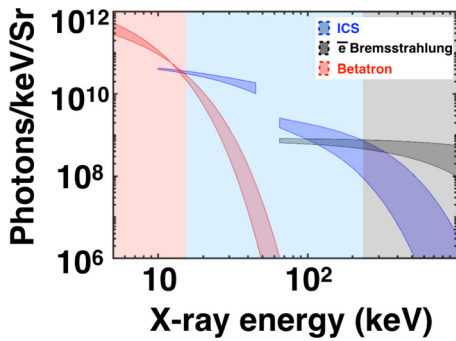


FIG. 9. The highest yield spectra for betatron radiation (red), ICS (blue), and electron bremsstrahlung radiation (black). The vertical red, blue, and black regions denote the photon energies where the betatron, ICS, and electron bremsstrahlung radiation dominate the x-ray spectra, respectively.

material. This versatility can be particularly useful for opacity/radiography measurements at HED facilities that can require photon energies up to a few MeV to study high-Z materials in HED conditions or for imaging double-shell ignition targets. Further improvements to this source are still possible, as it was found that the source size can be approximated by the size of the electron beam hitting the foil. Thus, the source size can be controlled by changing the distance from the electron source to the converter foil or by reducing the size of the converter foil (using high-Z thin wires).

ICS radiation was generated by an LPA using a ps, kJ-class laser and a plasma mirror. Photon energies from 10 to 250 keV were generated with photon yields from 10^{10} to 10^9 photons/keV/Sr, respectively. Integrating the energy spectrum, a total number of 10^{11} photons per shot were generated, representing an improvement of three orders of magnitude when compared to the best ICS-LPA results obtained in the blowout regime.³⁶ An estimated source size of 50 μm and a divergence of 100 mrad were measured. This source as the potential to be very useful for HED since for the first time an ICS source based on LPA reaches the necessary photon yields to radiograph high-areal density objects and matter under extreme conditions in a single shot. A direct comparison of the photon energy spectra for each of these sources can be seen in Fig. 9. It is clear that each one of these mechanisms dominates over the other for different photon energies. The betatron radiation has a higher yield up to photon energies of 20 keV, followed by ICS from 20 to 200 keV, and bremsstrahlung radiation for energies higher than 200 keV.

Table I shows a summary of the characteristics of the sources based on LPA driven by a ps, kJ-class laser. In conclusion, depending

TABLE I. Table denotes the characteristics of each source.

	Photon energies with higher yield than the other mechanisms (keV)	Source size (μm)	Divergence (μm)
Betatron	1–20	<35	100–200
Inv. Comp. Scatt.	20–200	~50	~100
Bremsstrahlung	>200	100–1000 ^a	220 ^a

^aValues from Monte Carlo simulations.

on the application needs, one can elect which mechanism to use, simply by choosing the foil at the end of the gas jet. Future improvements to these sources can be envisioned by scaling to higher laser energies or by combining the ICS and bremsstrahlung mechanisms using a plasma mirrors attached to a high-Z material.

ACKNOWLEDGMENTS

This work was performed under the auspices of the U.S. Department of Energy under Contract No. DE-AC52-07NA27344 and supported by the Laboratory Directed Research and Development (LDRD) Program under tracking codes 16-ERD-024 at LLNL and by the joint NNSA/DOE program Grant No. DE-NA0002950 at UCLA. F.A. acknowledges support from the DOE Office of Science Early Career Research Program under SCW1575-1. B.M.H. and P.K. acknowledge support from the Air Force Office of Scientific Research (AFOSR) under Grant No. FA9550-17-1-0264. B.M.H. acknowledges support by the Institute of Basic Science (IBS) under Grant No. IBS-R012-D1 and from GIST Research Institute (GRI) grant 2018. J.L.S. acknowledges support from the U.S. Department of Energy under Award No. DE-SC0017950, the National Science Foundation under Award No. PHY-1705224, and the Department of Energy National Nuclear Security Administration under Award No. DE-NA0003856. The authors thank R. C. Cauble, S. Andrews, B. Stuart, R. Costa, C. Bruns, C. Cadwalader, and S. Maricle for their support of the Titan laser system at the Jupiter Laser Facility. LLNL-JRNL-767264-DRAFT.

REFERENCES

1. Lindl, “Development of the indirect-drive approach to inertial confinement fusion and the target physics basis for ignition and gain,” *Phys. Plasmas* **2**, 3933–4024 (1995).
2. B. A. Remington, “High energy density laboratory astrophysics,” *Plasma Phys. Controlled Fusion* **47**, A191–A203 (2005).
3. C. Courtois, R. Edwards, A. Compant La Fontaine, C. Aedy, S. Bazzoli, J. L. Bourgade, J. Gazave, J. M. Lagrange, O. Landoas, L. L. Dain, D. Mastro Simone, N. Pichoff, G. Pien, and C. Stoeckl, “Characterisation of a MeV Bremsstrahlung x-ray source produced from a high intensity laser for high areal density object radiography,” *Phys. Plasmas* **20**, 083114 (2013).
4. M. D. Perry, J. A. Sefcik, T. Cowan, S. Hatchett, A. Hunt, M. Moran, D. Pennington, R. Snavely, and S. C. Wilks, “Hard x-ray production from high intensity laser solid interactions (invited),” *Rev. Sci. Instrum.* **70**, 265–269 (1999).
5. P. A. Norreys, M. Santala, E. Clark, M. Zepf, I. Watts, F. N. Beg, K. Krushelnick, M. Tatarakis, A. E. Dangor, X. Fang, P. Graham, T. McCanny, R. P. Singhal, K. W. D. Ledingham, A. Creswell, D. C. W. Sanderson, J. Magill, A. Machacek, J. S. Wark, R. Allott, B. Kennedy, and D. Neely, “Observation of a highly directional γ -ray beam from ultrashort, ultraintense laser pulse interactions with solids,” *Phys. Plasmas* **6**, 2150–2156 (1999).
6. S. P. Hatchett, C. G. Brown, T. E. Cowan, E. A. Henry, J. S. Johnson, M. H. Key, J. A. Koch, A. B. Langdon, B. F. Lasinski, R. W. Lee, A. J. Mackinnon, D. M. Pennington, M. D. Perry, T. W. Phillips, M. Roth, T. C. Sangster, M. S. Singh, R. A. Snavely, M. A. Stoyer, S. C. Wilks, and K. Yasuike, “Electron, photon, and ion beams from the relativistic interaction of Petawatt laser pulses with solid targets,” *Phys. Plasmas* **7**, 2076–2082 (2000).
7. J. C. Fernández, D. Cort Gautier, C. Huang, S. Palaniyappan, B. J. Albright, W. Bang, G. Dyer, A. Favalli, J. F. Hunter, J. Mendez, M. Roth, M. Swinhoe, P. A. Bradley, O. Deppert, M. Espy, K. Falk, N. Guler, C. Hamilton, B. M. Hegelich, D. Henzlova, K. D. Ianakiev, M. Iliev, R. P. Johnson, A. Kleinschmidt, A. S. Losko, E. McCary, M. Mocko, R. O. Nelson, R. Roycroft, M. A. Santiago Cordoba, V. A. Schanz, G. Schaumann, D. W. Schmidt, A. Sefkow, T. Shimada, T. N. Taddeucci, A. Tebartz, S. C. Vogel, E. Vold, G. A. Wurden, and

- L. Yin, "Laser-plasmas in the relativistic-transparency regime: Science and applications," *Phys. Plasmas* **24**, 056702 (2017).
- ⁸J. D. Hares, J. D. Kilkenny, M. H. Key, and J. G. Lunney, "Measurement of fast-electron energy spectra and preheating in laser-irradiated targets," *Phys. Rev. Lett.* **42**, 1216–1219 (1979).
- ⁹H. Chen, B. Soom, B. Yaakobi, S. Uchida, and D. D. Meyerhofer, "Hot-electron characterization from k α measurements in high-contrast, p-polarized, picosecond laser-plasma interactions," *Phys. Rev. Lett.* **70**, 3431–3434 (1993).
- ¹⁰A. Rousse, P. Audebert, J. P. Geindre, F. Falliès, J. C. Gauthier, A. Mysyrowicz, G. Grillon, and A. Antonetti, "Efficient k α x-ray source from femtosecond laser-produced plasmas," *Phys. Rev. E* **50**, 2200–2207 (1994).
- ¹¹A. B. Sefkow, G. R. Bennett, M. Geissel, M. Schollmeier, B. C. Franke, and B. W. Atherton, "Efficiency enhancement for K α X-ray yields from laser-driven relativistic electrons in solids," *Phys. Rev. Lett.* **106**, 235002 (2011).
- ¹²H. S. Park, D. M. Chambers, H. K. Chung, R. J. Clarke, R. Eagleton, E. Giraldez, T. Goldsack, R. Heathcote, N. Izumi, M. H. Key, J. A. King, J. A. Koch, O. L. Landen, A. Nikroo, P. K. Patel, D. F. Price, B. A. Remington, H. F. Robey, R. A. Snavely, D. A. Steinman, R. B. Stephens, C. Stoeckl, M. Storm, M. Tabak, W. Theobald, R. P. J. Town, J. E. Wickersham, and B. B. Zhang, "High-energy K α radiography using high-intensity, short-pulse lasers," *Phys. Plasmas* **13**, 056309 (2006).
- ¹³B. Westover, A. MacPhee, C. Chen, D. Hey, T. Ma, B. Maddox, H. S. Park, B. Remington, and F. N. Beg, "Study of silver K α and bremsstrahlung radiation from short-pulse laser-matter interactions with applications for x-ray radiography," *Phys. Plasmas* **17**, 082703 (2010).
- ¹⁴F. Albert and A. G. R. Thomas, "Applications of laser wakefield accelerator-based light sources," *Plasma Phys. Controlled Fusion* **58**, 103001 (2016).
- ¹⁵S. Corde, K. T. Phuoc, G. Lambert, R. Fitour, V. Malka, A. Rousse, A. Beck, and E. Lefebvre, "Femtosecond x rays from laser-plasma accelerators," *Rev. Mod. Phys.* **85**, 1–48 (2013).
- ¹⁶E. Esarey, B. A. Shadwick, P. Catravas, and W. P. Leemans, "Synchrotron radiation from electron beams in plasma-focusing channels," *Phys. Rev. E* **65**, 056505 (2002).
- ¹⁷Y. Glinec, J. Faure, L. L. Dain, S. Darbon, T. Hosokai, J. J. Santos, E. Lefebvre, J. P. Rousseau, F. Burgy, B. Mercier, and V. Malka, "High-resolution γ -ray radiography produced by a laser-plasma driven electron source," *Phys. Rev. Lett.* **94**, 025003 (2005).
- ¹⁸A. Modena, Z. Najmudin, A. Dangor, C. Clayton, K. Marsh, C. Joshi, V. Malka, C. Darrow, C. Danson, D. Neely, and F. Walsh, "Electron acceleration from the breaking of relativistic plasma-waves," *Nature* **377**, 606–608 (1995).
- ¹⁹F. Albert, N. Lemos, J. L. Shaw, B. B. Pollock, C. Goyon, W. Schumaker, A. M. Saunders, K. A. Marsh, A. Pak, J. E. Ralph, J. L. Martins, L. D. Amorim, R. W. Falcone, S. H. Glenzer, J. D. Moody, and C. Joshi, "Observation of betatron X-ray radiation in a self-modulated laser wakefield accelerator driven with picosecond laser pulses," *Phys. Rev. Lett.* **118**, 134801 (2017).
- ²⁰N. Lemos, F. Albert, J. L. Shaw, D. Papp, R. Polanek, P. King, A. L. Milder, K. A. Marsh, A. Pak, B. B. Pollock, B. M. Hegelich, J. D. Moody, J. Park, R. Tommasini, G. J. Williams, H. Chen, and C. Joshi, "Bremsstrahlung hard x-ray source driven by an electron beam from a self-modulated laser wakefield accelerator," *Plasma Phys. Controlled Fusion* **60**, 054008 (2018).
- ²¹e. a. N. Lemos, "Ultrabroad-band, inverse Compton scattering source using a picosecond laser driven plasma accelerator," *Phys. Rev. Lett.* (submitted).
- ²²G. J. Williams, H. Chen, J. E. Field, O. L. Landen, and D. J. Strozzi, "Positron radiography of ignition-relevant icf capsules," *Phys. Plasmas* **24**, 122704 (2017).
- ²³F. V. Hartemann, *High-Field Electrodynamics* (CRC Press, 2001).
- ²⁴P. Catravas, E. Esarey, and W. P. Leemans, "Femtosecond x-rays from thomson scattering using laser wakefield accelerators," *Meas. Sci. Technol.* **12**, 1828–1834 (2001).
- ²⁵F. V. Hartemann, D. J. Gibson, W. J. Brown, A. Rousse, K. T. Phuoc, V. Malka, J. Faure, and A. Pukhov, "Compton scattering x-ray sources driven by laser wakefield acceleration," *Phys. Rev. Spec. Top.-Accel. Beams* **10**, 011301 (2007).
- ²⁶G. R. Bennett, M. E. Cuneo, R. A. Vesey, J. L. Porter, R. G. Adams, R. A. Aragon, J. A. Caird, O. L. Landen, P. K. Rambo, D. C. Rovang, L. E. Ruggles, W. W. Simpson, I. C. Smith, and D. F. Wenger, "Symmetric inertial-confinement-fusion-capsule implosions in a double-z-pinch-driven hohlraum," *Phys. Rev. Lett.* **89**, 245002 (2002).
- ²⁷A. Schropp, R. Hoppe, V. Meier, J. Patommel, F. Seiboth, Y. Ping, D. G. Hicks, M. A. Beckwith, G. W. Collins, A. Higginbotham, J. S. Wark, H. J. Lee, B. Nagler, E. C. Galtier, B. Arnold, U. Zastra, J. B. Hastings, and C. G. Schroer, "Imaging shock waves in diamond with both high temporal and spatial resolution at an XFEL," *Sci. Rep.* **5**, 11089 (2015).
- ²⁸D. E. Eakins and D. J. Chapman, "X-ray imaging of subsurface dynamics in high-Z materials at the Diamond Light Source," *Rev. Sci. Instrum.* **85**, 123708 (2014).
- ²⁹S. Chen, G. Golovin, C. Miller, D. Haden, S. Banerjee, P. Zhang, C. Liu, J. Zhang, B. Zhao, S. Clarke, S. Pozzi, and D. Umstadter, "Shielded radiography with a laser-driven MeV-energy X-ray source," *Nucl. Instrum. Methods Phys. Res., Sect. B* **366**, 217–223 (2016).
- ³⁰J. C. Wood, D. J. Chapman, K. Poder, N. C. Lopes, M. E. Rutherford, T. G. White, F. Albert, K. T. Behm, N. Booth, J. S. J. Bryant, P. S. Foster, S. Glenzer, E. Hill, K. Krushelnick, Z. Najmudin, B. B. Pollock, S. Rose, W. Schumaker, R. H. H. Scott, M. Sherlock, A. G. R. Thomas, Z. Zhao, D. E. Eakins, and S. P. D. Mangles, "Ultrafast imaging of laser driven shock waves using betatron X-rays from a laser wakefield accelerator," *Sci. Rep.* **8**, 11010 (2018).
- ³¹J. L. Shaw, N. Lemos, L. D. Amorim, N. Vafaei-Najafabadi, K. A. Marsh, F. S. Tsung, W. B. Mori, and C. Joshi, "Role of direct laser acceleration of electrons in a laser wakefield accelerator with ionization injection," *Phys. Rev. Lett.* **118**, 064801 (2017).
- ³²A. Pukhov, Z.-M. Sheng, and J. Meyer-ter Vehn, "Particle acceleration in relativistic laser channels," *Phys. Plasmas* **6**, 2847 (1999).
- ³³J. L. Shaw, F. S. Tsung, N. Vafaei-Najafabadi, K. A. Marsh, N. Lemos, W. B. Mori, and C. Joshi, "Role of direct laser acceleration in energy gained by electrons in a laser wakefield accelerator with ionization injection," *Plasma Phys. Controlled Fusion* **56**, 084006 (2014).
- ³⁴X. Zhang, V. N. Khudik, and G. Shvets, "Synergistic laser-wakefield and direct-laser acceleration in the plasma-bubble regime," *Phys. Rev. Lett.* **114**, 184801 (2015).
- ³⁵G. Doumy, F. Quéré, O. Gobert, M. Perdrix, P. Martin, P. Audebert, J. C. Gauthier, J. P. Geindre, and T. Wittmann, "Complete characterization of a plasma mirror for the production of high-contrast ultraintense laser pulses," *Phys. Rev. E* **69**, 026402 (2004).
- ³⁶K. T. Phuoc, S. Corde, C. Thaurv, V. Malka, A. Tafzi, J. P. Goddet, R. C. Shah, S. Sebban, and A. Rousse, "All-optical Compton gamma-ray source," *Nat. Photonics* **6**, 308–311 (2012).
- ³⁷H.-E. Tsai, X. Wang, J. M. Shaw, Z. Li, A. V. Arefiev, X. Zhang, R. Zgadzaj, W. Henderson, V. Khudik, G. Shvets, and M. C. Downer, "Compact tunable Compton x-ray source from laser-plasma accelerator and plasma mirror," *Phys. Plasmas* **22**, 023106 (2015).
- ³⁸R. W. Schoenlein, W. P. Leemans, A. H. Chin, P. Volfbeyn, T. E. Glover, P. Balling, M. Zolotarev, K. J. Kim, S. Chattopadhyay, and C. V. Shank, "Femtosecond X-ray pulses at 0.4 Å generated by 90° Thomson scattering: A tool for probing the structural dynamics of materials," *Science* **274**, 236–238 (1996).
- ³⁹E. Esarey, P. Sprangle, J. Krall, and A. Ting, *IEEE Trans. Plasma Sci.* **24**, 252–288 (1996).
- ⁴⁰N. Lemos, J. L. Martins, F. S. Tsung, J. L. Shaw, K. A. Marsh, F. Albert, B. B. Pollock, and C. Joshi, "Self-modulated laser wakefield accelerators as x-ray sources," *Plasma Phys. Controlled Fusion* **58**, 034018 (2016).
- ⁴¹R. D. Edwards, M. A. Sinclair, T. J. Goldsack, K. Krushelnick, F. N. Beg, E. L. Clark, A. E. Dangor, Z. Najmudin, M. Tatarakis, B. Walton, M. Zepf, K. W. D. Ledingham, I. Spencer, P. A. Norreys, R. J. Clarke, R. Kodama, Y. Toyama, and M. Tampo, "Characterization of a gamma-ray source based on a laser-plasma accelerator with applications to radiography," *Appl. Phys. Lett.* **80**, 2129 (2002).
- ⁴²N. D. Powers, I. Ghebregziabher, G. Golovin, C. Liu, S. Chen, S. Banerjee, J. Zhang, and D. P. Umstadter, "Quasi-monoenergetic and tunable X-rays from a laser-driven Compton light source," *Nat. Photonics* **8**, 28–31 (2014).
- ⁴³K. Chouffani, D. Wells, F. Harmon, J. Jones, and G. Lancaster, "Laser-Compton scattering from a 20 MeV electron beam," *Nucl. Instrum. Methods Phys. Res., Sect. A* **495**, 95–106 (2002).
- ⁴⁴N. Lemos, N. Lopes, J. M. Dias, and F. Viola, "Design and characterization of superionic nozzles for wide focus laser-plasma interactions," *Rev. Sci. Instrum.* **80**, 103301 (2009).
- ⁴⁵S. Semushin and V. Malka, *Rev. Sci. Instrum.* **72**, 2961 (2001).
- ⁴⁶A. Pak, K. Marsh, S. Martins, W. Lu, W. Mori, and C. Joshi, *Phys. Rev. Lett.* **104**, 025003 (2010).

- ⁴⁷N. Lemos, L. Cardoso, J. Geada, G. Figueira, F. Albert, and J. M. Dias, "Guiding of laser pulses in plasma waveguides created by linearly-polarized femtosecond laser pulses," *Sci. Rep.* **8**, 3165 (2018).
- ⁴⁸C. D. Chen, J. A. King, M. H. Key, K. U. Akli, F. N. Beg, H. Chen, R. R. Freeman, A. Link, A. J. Mackinnon, A. G. MacPhee, P. K. Patel, M. Porkolab, R. B. Stephens, and L. D. Van Woerkom, "A Bremsstrahlung spectrometer using k-edge and differential filters with image plate dosimeters," *Rev. Sci. Instrum.* **79**, 10E305-4 (2008).
- ⁴⁹G. J. Williams, R. Tommasini, N. Lemos, J. Park, and H. Chen, "High-energy differential-filtering photon spectrometer for ultraintense laser-matter interactions," *Rev. Sci. Instrum.* **89**, 10F116-6 (2018).
- ⁵⁰P. Kirkpatrick, "On the theory and use of ross filters," *Rev. Sci. Instrum.* **10**, 186-191 (1939).
- ⁵¹P. M. King, N. Lemos, J. L. Shaw, A. L. Milder, K. A. Marsh, A. Pak, B. M. Hegelich, P. Michel, J. Moody, C. Joshi, and F. Albert, *Rev. Sci. Instrum.* **90**(3), 033503 (2019).
- ⁵²C. Thaury, E. Guillaume, S. Corde, R. Lehe, M. L. Bouteiller, K. T. Phuoc, X. Davoine, J. M. Rax, A. Rouse, and V. Malka, "Angular-momentum evolution in laser-plasma accelerators," *Phys. Rev. Lett.* **111**, 135002 (2013).
- ⁵³S. P. D. Mangles, A. G. R. Thomas, M. C. Kaluza, O. Lundh, F. Lindau, A. Persson, F. S. Tsung, Z. Najmudin, W. B. Mori, C.-G. Wahlström, and K. Krushelnick, "Laser-wakefield acceleration of monoenergetic electron beams in the first plasma-wave period," *Phys. Rev. Lett.* **96**, 215001 (2006).
- ⁵⁴C. D. Chen, P. K. Patel, D. S. Hey, A. J. Mackinnon, M. H. Key, K. U. Akli, T. Bartal, F. N. Beg, S. Chawla, H. Chen, R. R. Freeman, D. P. Higginson, A. Link, T. Y. Ma, A. G. MacPhee, R. B. Stephens, L. D. Van Woerkom, B. Westover, and M. Porkolab, "Bremsstrahlung and K α fluorescence measurements for inferring conversion efficiencies into fast ignition relevant hot electrons," *Phys. Plasmas* **16**, 082705 (2009).
- ⁵⁵L. C. Jarrott, A. J. Kemp, L. Divol, D. Mariscal, B. Westover, C. McGuffey, F. N. Beg, M. Suggit, C. Chen, D. Hey, B. Maddox, J. Hawreliak, H. S. Park, B. Remington, M. S. Wei, and A. MacPhee, "K α and bremsstrahlung x-ray radiation backlighter sources from short pulse laser driven silver targets as a function of laser pre-pulse energy," *Phys. Plasmas* **21**, 031211 (2014).
- ⁵⁶A. Lévy, F. Dorchies, M. Harmand, C. Fourment, S. Hulin, O. Peyrusse, J. J. Santos, P. Antici, P. Audebert, J. Fuchs, L. Lancia, A. Mancic, M. Nakatsutsumi, S. Mazevet, V. Recoules, P. Renaudin, and S. Fourmaux, "X-ray absorption for the study of warm dense matter," *Plasma Phys. Controlled Fusion* **51**, 124021 (2009).